

Unveiling Molecular Moieties through Hierarchical Graph Explainability

Paolo Sortino^{1,‡}, Salvatore Contino^{1,*‡}, Ugo Perricone^{2,*}, Roberto Pirrone¹

February 6, 2024

Abstract

Background: Graph Neural Networks (GNN) have emerged in very recent years as a powerful tool for supporting *in silico* Virtual Screening. In this work we present a GNN which uses Graph Convolutional architectures to achieve very accurate multi-target screening. We also devised a hierarchical Explainable Artificial Intelligence (XAI) technique to catch information directly at atom, ring, and whole molecule level by leveraging the message passing mechanism. In this way, we find the most relevant moieties involved in bioactivity prediction.

Results: We report a state-of-the-art GNN classifier on twenty Cyclin-dependent Kinase targets in support of VS. Our classifier outperforms previous SOTA approaches proposed by the authors. Moreover, a CDK1-only high-sensitivity version of the GNN has been designed to use our explainer in order to avoid the inherent bias of multi-class models. The hierarchical explainer has been validated by an expert chemist on 19 approved drugs on CDK1. Our explainer provided information in accordance to the docking analysis for 17 out of the 19 test drugs.

Conclusion: Our approach is a valid support for shortening both the screening and the hit-to-lead phase. Detailed knowledge about the molecular substructures that play a role in the inhibitory action, can help the computational chemist to gain insights into the pharmacophoric function of the molecule also for repurposing purposes.

1 Background

The development of a new drug is a long and time-consuming process that, despite advances in technology and computer applications, is fragmented into several steps before being able to identify a lead compound that can be tested on *in vivo* models. Over the last decade, the use of deep learning has provided support to the Virtual Screening (VS) campaigns for the efficient selection of hit compounds by strengthening predictions through the use of massive data in the training model phase [11, 4, 22, 3, 29]. Indeed, being able to correctly prioritise active molecules during the screening steps speeds up the discovery process. Classical approaches used in CADD are not always efficient, being affected by the use of specific force field [21, 13]

*corresponding author salvatore.contino01@unipa.it (Salvatore Contino), uperricone@fondazionerimed.com (Ugo Perricone)

‡These authors contributes equally.

¹Department of Engineering, University of Palermo, 90128 Palermo, Italy

²Molecular Informatics Group, Fondazione Ri.MED, 90128 Palermo, Italy

and the quality of structural data available, thus affecting the hit optimisation steps towards the lead compound. Hit discovery is the very first step after screening, and chemists use it as the starting point to optimise hits rationally until designing a lead compound. This step uses different techniques such as hit expansion, (bio)isosteric replacement or a combination of them [10]. Hit expansion, for instance, is one of the most widely used techniques for optimisation and it is based on the synthesis of analogues to the selected small molecule by replacing chemical patterns, guided by data obtained from Structure Activity Relationship (SAR) analysis [2]. (Bio)isosteric replacement is a technique based on the definition of isoterism introduced by Langmuir in 1919, during his studies of the physicochemical properties of atoms and chemical groups. He noted that atoms with similar properties trigger the same biological effect; for example, compounds with the same number of atoms and electrons (e.g. N_2 , CO, N_2O , etc.) are isosteric and trigger the same biological behaviour. On the basis of the same electron arrays, the chemical groups have been divided into 21 groups that are used to optimise bioactive molecules by increasing their efficiency as [7] drugs. Clearly, optimisation requires an understanding of the relevant atoms or chemical groups within the small molecule. This step is usually handled by the computational chemist, who recognizes and consciously acts to improve the molecule’s activity in accordance with their knowledge and expertise in the field.

In this context, Graph Neural Networks (GNN) [18, 12] have emerged as powerful tools in Drug Discovery and Virtual Screening due to their ability to model complex molecular structures and interactions. By leveraging the graph-based representation of molecules to capture local and global structural information, GNNs offer a promising approach for predicting molecular properties, bioactivity and drug-target interactions [9, 28, 24, 26, 20, 5, 23].

In the present work, we are presenting a GNN based on the so called Graph Convolutional layers, which firstly prioritise molecules towards a set of 20 kinases with a very high rate of precision, and also supports the computational chemist in the selection of the most important chemical features in the host-guest recognition. The proposed neural architecture provides a very good bioactivity classification (F_1 score > 98% on average). Moreover, we devised a suitable Explainable AI (XAI) procedure, which is inspired to the well known Gradient-weighted Class Activation Mapping (Grad-CAM) [19]. Grad-CAM is an explainer used in image classification through Convolutional Neural Networks (CNN) and it generates a heatmap for each class to highlight the parts of an image that contribute to the recognition of that class. At each layer where Grad-CAM is applied, the role of each feature map in explaining the class is weighted using the gradients back propagated to the layer itself. In [16] a graph based version of Grad-CAM is proposed, and we used this implementation for our molecular explainer that provides a graphical representation highlighting the atoms and/or chemical groups with a key role in the discriminative event. We used the four macro-groups of pharmacophoric features (H-bond donor or acceptor, hydrophobic, aromatic) [6] in this respect.

In general, Grad-CAM is applied only to the last layer of the classifier whose feature maps convey aggregated position-independent information on the features extracted by the deep layers of the network. Rather than providing a global explanation of the classifier behaviour, the key idea behind our approach is trying to explain how the different molecular moieties are involved in predicting a high degree bioactivity. These structures are expected to play a crucial role in binding to the target. As a consequence, we used a hierarchy of explainers placed at different layers to catch information directly at atom, ring, and whole molecule level by leveraging the message passing mechanism that is used in GNNs. The explainer hierarchy for a target is applied purposely to a binary version of our classifier. Such a network has a similar layer arrangement as the 20-target network, but the layers’ sizes have been designed ad hoc,

and a novel training on the selected target has been performed to achieve high accuracy, while avoiding the inherent bias of a multi-target prediction with respect to the different classes. In this paper we present the implementation of the whole explainability procedure for CDK1, which is a well-known regulator of the cell cycle, and has a crucial role in tumor genesis. Our explainability results for nineteen well known drugs that are active on CDK1 were manually validated by expert computational chemists, and this was a very time consuming task. The proposed approach is exactly the same for each target so this choice does not reduce the generality of our results.

2 Methods

All the experiments presented in this work were carried on using a data set which was built by some of the authors [14] and contains small molecules that are active on twenty Kinases. We selected this data set as it was used by a deep neural classifier that leverages the *EMBER* molecular descriptor based on molecular fingerprints. Such a classifier provides state-of-the-art performance both in classification accuracy and Enrichment Factor (EF) values for screening tasks. Even if molecular fingerprints are a well known descriptor, they are not prone to provide explicit information about the single moieties involved in bioactivity, and we started our explainability study from a comparison between fingerprint and graph descriptors. As a consequence, we built a graph version of the twenty target classifier: we expected an increased performance using graphs due to their one-to-one encoding of the chemical information about atoms and bonds, and our prevision was supported by the experimental results. Next, we moved towards a fine explanation of the role of each molecular moiety in the prediction, and the hierarchical explainer was devised in this respect.

2.1 Data preparation

Input molecular graphs for our neural architecture were generated from the canonical SMILES representation. Unlike the other molecular descriptors used in classical approaches for Virtual Screening, molecular graphs account for chemical information both in each atom and its chemical neighborhood. Each node represents an atom as a feature vector, and nine features were selected in the proposed representation:

- Atomic number
- Degree
- Formal Charge
- Hybridization
- Aromaticity
- Total number of hydrogen atoms
- Number of radical electrons
- Information on aromaticity
- Chirality

The set of atom features was later augmented with the 3D coordinates of each atom in active configuration, for the sake of training the single-class architecture used for the hierarchical explainability analysis. These coordinates were calculated by maximising the local minimum of the active conformation for each individual molecule. Edges information concerns the type of bond (double or triple bond) and whether the bond is within a cycle. The size of each molecular graph had several nodes and arcs which vary according to the size of the molecule.

Canonical SMILES were recovered from ChEMBL [1] for all the small molecules whose activity on the target protein is referenced by IC₅₀, K_i, and K_d values. We used a fixed threshold activity value on each target, in order to generate the molecular graphs through the use of the RDKit library, which allows obtaining all the features previously described. The final dataset consists of 89373 small molecules and has a 1:100 active/inactive ratio for the smallest class that is CLK2. This ratio allows profound assessing of the model generalization abilities as it has more or less the same size of a real world screening task. Training, validation, and test sets were created using a 80%:10%:10% ratio for each target, in order to minimize the comparison bias.

2.2 Graph Convolutional Neural Network

The neural architecture used in this study is made by two main parts: the Graph Convolutional (GC) blocks, and the true classifier which uses dense layers. As reported before, the multi-target, and the single target network share the same arrangement as regards the two parts but with different sizes for each single layer. In the multi-target network, seven GC blocks are employed. Each block consists of a proper GC layer that implements the *1-dimensional Weisfeler-Leman kernel* (1-WL) and has been presented in [15]. Such a layer uses the message-passing algorithm [8] to collect information from the direct neighbors of each node. After the GC layer, each block contains a Rectified Linear Unit (ReLU) activation function and a Layer normalization operation. The primary goal of a GC block is using both the node and the adjacency matrix to collect relevant features from neighboring nodes within the graph.

The message-passing algorithm stacks data coming from neighbours, for each node in the graph. This aggregation process results in an updated set of node features placed along the channel dimension of the data sample. More formally, the algorithm uses a message function M_t and a vertex update function U_t , which is usually implemented as a Multi Layer Perceptron (MLP). Both those functions are learnable and differentiable in order to be trained in a neural network. Given the time-step t , the node v collecting features, the edge e_{vw} connecting node v and any node w in the set $N(v)$ of the neighbors of v in the graph G , and the hidden states h_v^t and h_w^t , the new message m_v at time-step $t + 1$ is calculated as shown in eq. 1.

$$(1) \quad m_v^{t+1} = \sum_{w \in N(v)} M_t(h_v^t, h_w^t, e_{vw})$$

The new hidden state h_v^{t+1} is then computed using the previous hidden state h_v^t and the new message m_v^{t+1} , shown in eq. 2.

$$(2) \quad h_v^{t+1} = U_t(h_v^t, m_v^{t+1})$$

For the sake of rich feature extraction, the design the GC layers involved a systematic increase of the number of channels that are progressively doubled in a geometric progression:

32, 64, 128, 256, 512, and 1024. The purpose of this channel augmentation is to yield a more and more meaningful latent representation of the inputs, that is a critical aspect for achieving superior performance in the context of a multi-class classification task involving twenty distinct targets. The augmented node feature vector coming from the graph convolutional operations flows into a Global Average Pooling (GAP) layer. This step is also known as the *readout phase*, and it represents a core operation when using the message-passing algorithm. GAP condenses the information about all the nodes into a one-dimensional vector that averages all the features of the whole graph into a compressed and meaningful vector representation.

The second part of the multi-target network is a neural classifier consisting in four fully connected layers designed for both dimensionality reduction and features manipulation. The original size of 1024 features in the latent representation is reduced sequentially to 512, 256, 64, and 20 channels. ReLU activation functions and dropout layers are also added for each fully connected layer to add non-linearity correlation to the input data. Actual classification is achieved through a sigmoid activation function that rescales the incoming vector into a set of twenty independent probabilities for the input molecule to be active separately on each of the different targets. The whole architecture of the network is reported in 1.

The single target architecture differs significantly from the first one as regards both the number and the size of each layer. It is well known that the global efficacy of a model for Virtual Screening is measured through the ability of correctly prioritizing the *True Positives*, so the main aim of the network is providing a very high sensitivity with respect to the inhibitors of the target that is CDK1 in our experiments. In turn, stressing the network towards high sensitivity performance, makes it able to provide precise explanations about the molecular moieties involved in the inhibition. To achieve this result we operated in two ways: enrichment of the information encoded at each node, and accurate design of the model capacity through a change in the dimensions of the layers. The 3-D coordinates of each atom were computed by maximising the local minimum of the active conformation of the molecule, and they were added to the node features. Moreover, we selected a tighter network than the multi-target one because the task is only a binary classification.

The GC layers in the single target network elaborate the features in a U-Net [17] fashion, first enlarging, and then tightening the channels at each layer until a final 32 features representation is obtained. Seven GC blocks are used where the channels of each GC layer are arranged as follows: 32, 64, 128, 256, 128, 64, and again 32. Layer normalization and ReLU are obviously used in each block. After the GAP, four fully connected layers were used whose channels are respectively 2, 32, 16, and finally 1 that is fed to a sigmoid to estimate the probability for the input to be active on the target. The whole architecture of the single target network is reported in figure 2 along with an example of the output of the explainers used in the proposed hierarchy.

Both the neural architectures were trained using Weighted Binary Cross-Entropy with a higher weight value for the positives given the strong imbalance between active and inactive classes on targets. In both cases, a grid search was performed to select the hyperparameters properly. The number of GC filters was searched for in the set [1024, 512, 256, 128, 64, 32, 16], learning rates were in the range $[10^{-5}, 10^{-1}]$. The batch size ranged in [8, 64]. Model checkpoint was used to store the best model after each epoch and the early stopping procedure was utilized to determine the ideal number of training epochs. Hyperparameter optimization process took 64 days, and it was carried out on a NVIDIA GeForce RTX 3090 with 10496 CUDA Cores. Despite the low architecture complexity, each training session took roughly 8 hours because of the huge computation involved in the GC layers.

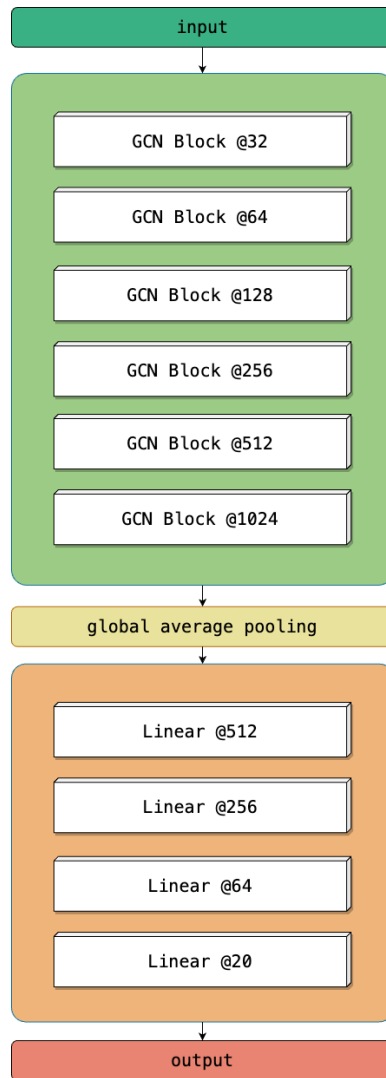


Figure 1: The architecture of the multi-target network

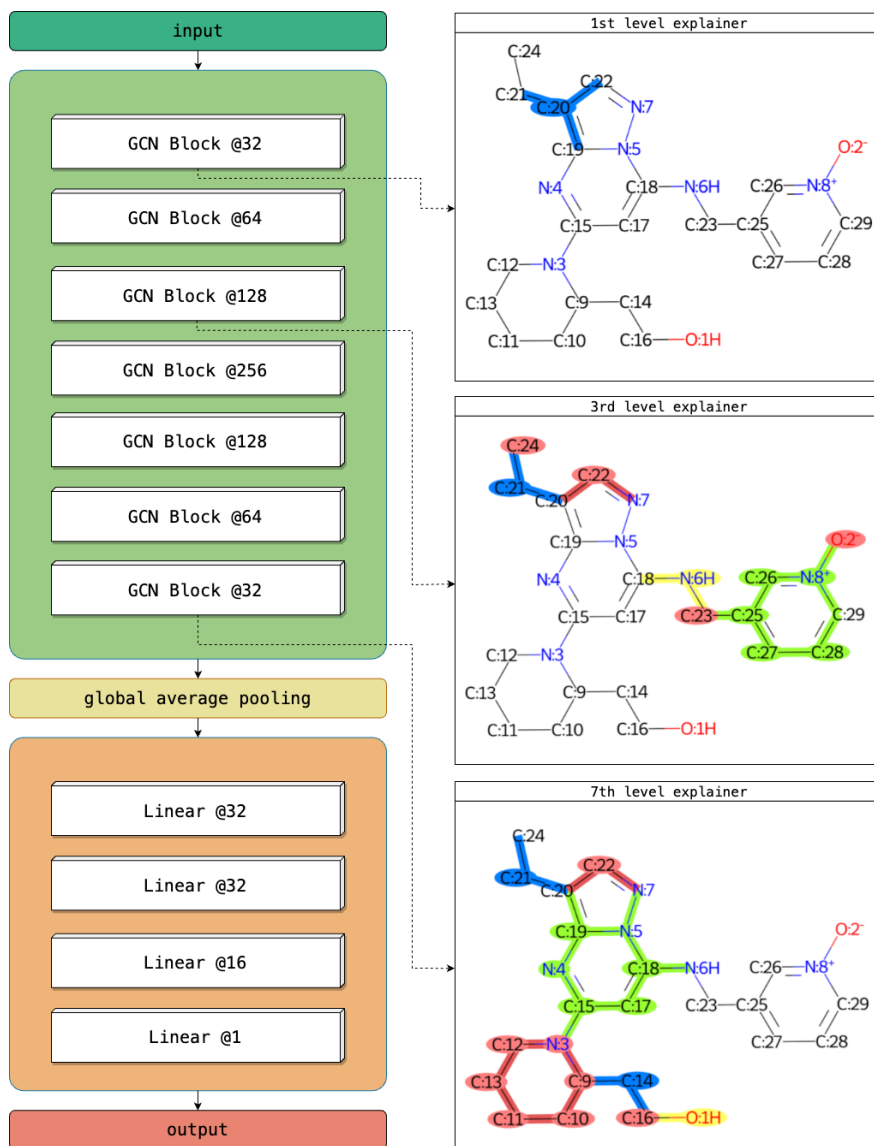


Figure 2: The architecture of the single-target network where the explainers for each level of the hierarchy are reported

2.3 Explainability analysis

Explainable AI (XAI) techniques were chosen to explore the black box of operations underlying neural network prediction. In the proposed work, XAI algorithms were used to be able to identify the parts of the small molecule directly involved in bioactivity. In fact, each hit molecule consists of groups with relevant activity in the interaction with the target that can be labelled as pharmacophoric.

Two different explainability tools were considered for the evaluation of the network results. Both are part of the so-called "Instance-level methods", i.e. those that provide a solution by identifying the most important input features that contribute most to the prediction. One of them, GNNExplainer [27], was picked because it is a "perturbation-based method" that tracks the change in output for minor variations of the same input data to determine which features are most important for prediction. However, this approach simply offers the graph arcs' contributions to the label prediction. Due to this, a second technique from the class of "Gradient and Feature-based techniques" was selected. With this method, a high gradient or higher values in the feature maps suggest that such features have a larger importance for the predictions. The goal is to use the gradient or hidden feature maps of the model to show the importance of input features.

An implementation from the work of Pope et Al. [16] was utilized for this purpose. In this work, the authors implemented some graph-based counterparts of three well-established explainability methods originally designed for convolutional neural networks. Among those, Gradient-weighted Class Activation Mapping (GradCAM) [19] has been chosen as the most representative of relevant input features for prediction. This method aims to visualize the region that activate most strongly when the network makes prediction for a particular class. It is done by examining the gradients of the target class score with respect to the feature map in the network.

The formula for calculating the weights α_k^l , related to layer l , node k and number of channels n of the feature maps $F_{k,n}^l$, is shown in eq. 3.

$$(3) \quad \alpha_k^l = \frac{1}{N} \sum_{n=1}^N \frac{\partial y}{\partial F_{k,n}^l}$$

Grad-CAM values for each node k is then calculated as described here in eq. 4.

$$(4) \quad L_{Grad-CAM}[l, n] = \sum_k \alpha_k^l F_{k,n}^l$$

The original Grad-CAM implementation has been modified to be optimized and suited for this task. First of all, unlike from the original implementation, the ReLU activation function has been removed. The decision was made to capture not only positive contributions to the prediction using Grad-CAM values but to include contributions from both negative and positive influences. Far from the image-related task of the original implementation, our explainability goal is to get information about pharmacophoric features of the input graph and not just insights about biological activity of the molecule.

The analysis of the features importance has been conducted performing the GradCAM evaluation multiple times, each time referring to a different "level" of depth of the convolutional segment of the network. In a graph convolutional neural network, the message-passing algorithm is crucial for the information retrieval. For each step of the graph convolution layer,

a message representing knowledge about neighbours is aggregated into the channel dimension of each node. In this scenario of molecule activity prediction we first chose to use GradCAM to look at those contribution after the first round of graph convolutions, for considering the atoms’ impact for a 1-step neighbourhood. In the same way, we chose to look after the third and the seventh (last) convolutional operation. In this second case, we want to highlight contribution for a 3-step neighbourhood, focusing on chemical structures that could be identified with a 3-step path for each of the atoms, such as rings. Focusing on the output of the last convolution, we make sure that we can have contribution for a 7-step path starting from each of the atoms in the molecule.

3 Results

3.1 Multi-class multi-target classification

In this section results from the 20-target classifier are discussed. Two accuracy metrics are used to describe the network’s performance: first, **Global Balanced Accuracy** assesses the network’s ability to predict both active and inactive molecules, while **Sensitivity** (also named Recall) focuses solely on the network’s performance in correctly classifying active molecules. The **F1-score** quantifies how well the model can correctly identify positive instances (Recall) while avoiding false positives (Precision). On the other hand, the **ROC-AUC curve** measures the model’s ability to discriminate between positive and negative instances. The TP/P ratio is employed to assess the classifier’s ability to prioritize ligands, counting the correct predictions relative to the total positives in the top x% of the test set. Finally, the Enrichment Factor metric measures how many times the tested model outperforms a purely random process. Both TP/P and EF were calculated for 1, 2, 5 and 10% of the whole test set.

Results for the 20-target classifier are shown in table 1 and table 2.

The findings show that the network correctly identifies positive and negative samples in terms of balanced accuracy and sensitivity. The range of results for this last metric increased significantly from the earlier work [14], where it ranged between 0.22 and 0.84. Now sensitivity has an average value of 0.904, showing that it is much easier for the network to classify positive samples. F1-Score results show that the network is able to overcome the dataset imbalance while simultaneously reducing the number of false negatives and false positives. The use of a weighted cross entropy loss function and a soft F-score loss term each properly balanced worked fine for the classification task.

Results for metrics TP/P and EF are shown in Table 2. The percentage of test set considered for 1%, 2%, 5% and 10% are respectively 134, 268, 670 and 1340. Both TP/P and EF are close to the ones of the previous work [14].

Results in table 3 refer to the single target classifier performances on the CDK1 protein.

The results obtained with the multiclassifier are excellent in terms of sensitivity, outperforming the multiclassifier based on the embedding of molecular fingerprints proposed by the same authors in the paper Mendolia et al. [14] The comparison between the two results is summarised in Figure 3 showing the sensitivity for all targets. It is notable that especially for the case of CLK2 there was a consistent improvement in performance related to sensitivity metric, going from a value of (—) to a value of 0.938, as it is shown also in Table 1.

Protein	Bal. Accuracy	Sensitivity	F1-Score	AUC
ACK	0.891	0.811	0.979	0.983
ALK	0.929	0.893	0.972	0.987
CDK1	0.921	0.907	0.956	0.969
CDK2	0.932	0.950	0.940	0.971
CDK6	0.916	0.846	0.989	0.988
CHK1	0.923	0.912	0.954	0.977
CK2A1	0.942	0.911	0.979	0.989
CLK2	0.938	0.965	0.929	0.989
DYRK1A	0.913	0.847	0.983	0.986
EGFR	0.930	0.881	0.982	0.990
ERK2	0.927	0.935	0.941	0.977
GSK3B	0.903	0.847	0.970	0.978
INSR	0.893	0.823	0.974	0.977
IRAK4	0.930	0.931	0.953	0.979
ITK	0.928	0.958	0.921	0.981
JKA2	0.945	0.960	0.945	0.984
JNK	0.918	0.946	0.923	0.971
MAP2K1	0.944	0.926	0.969	0.991
MELK	0.916	0.874	0.969	0.982
PDK1	0.913	0.860	0.973	0.986
Avg	0.922	0.904	0.960	0.981

Table 1: Results table for 20 target classification

3.2 Single-target classification

The multi-target classification architecture was not suited to the explainability applications proposed by the authors. In fact, in order to be able to accurately identify the pharmacophoric groups that characterise high-priority molecules, a model trained on CDK1 has been created to reduce the bias provided by the different targets. Classification performance was assessed using the same metrics as described in the 3.1 section and is shown in table 3 and 4.

As can be observed, both Global Balanced accuracy and Sensitivity are higher than those obtained on the same target in the multiclassifier, while performance in terms of TP/P and EF remained consistent with that observed previously.

3.3 Explainability results

The XAI GRAD-CAM-like algorithm has been used to identify the molecular regions with the higher impact on the target assignment. As described in the section 2.3 the evaluation of gradients at three different depths was the main insight of the work presented. In fact, the message-passing mechanism aggregates node information at each GraphConvolution. In this way, the first level gathers information on individual atoms, the second level integrates the information with that of neighbouring nodes up to a maximum of 3 nodes, in order to identify functional groups, while with the last level the entire structure is taken into account, bringing out entire regions, commonly called molecular substructures, that actively contribute to the classification. An example of what is observed with the gradient analysis for the different depths is shown in figure 4, where the parts of the molecules with higher contribute are highlighted.

The figure 4 shows the atoms or their atomic groups which are identified as relevant to the

Protein	TP/P 1%	TP/P 2%	TP/P 5%	TP/P 10%	EF 1%	EF 2%	EF 5%	EF 10%
ACK	72/106	78/106	94/106	100/106	67	36	17	9
ALK	123/254	186/254	227/254	242/254	48	36	17	9
CDK1	80/205	117/205	177/205	190/205	39	28	17	9
CDK2	86/303	141/303	240/303	287/303	28	23	15	9
CDK6	82/104	89/104	94/104	99/104	78	42	18	9
INSR	89/217	123/217	180/217	204/217	41	28	16	9
ITK	98/158	127/158	145/158	154/158	62	40	18	9
JAK2	134/832	268/832	651/832	774/832	16	16	15	9
JNK3	79/105	83/105	93/105	102/105	75	39	17	9
MELK	125/185	158/185	171/185	179/185	67	42	18	9
CHK1	126/343	189/343	269/343	319/343	36	27	15	9
CK2A1	93/151	115/151	128/151	141/151	61	38	16	9
CLK2	52/102	63/102	85/102	96/102	50	30	16	9
DYRK1A	72/174	106/174	144/174	167/174	41	30	16	9
EGFR	129/702	262/702	520/702	641/702	18	18	14	9
ERK2	130/525	260/525	444/525	503/525	24	24	16	9
GSK3	102/393	174/393	293/393	358/393	25	22	14	9
IRAK4	134/339	249/339	311/339	327/339	39	36	18	9
MAP2K1	106/191	133/191	166/191	181/191	55	34	17	9
PDK1	108/187	132/187	164/187	183/187	57	35	17	9

Table 2: TP/P and EF values for 20 target classification

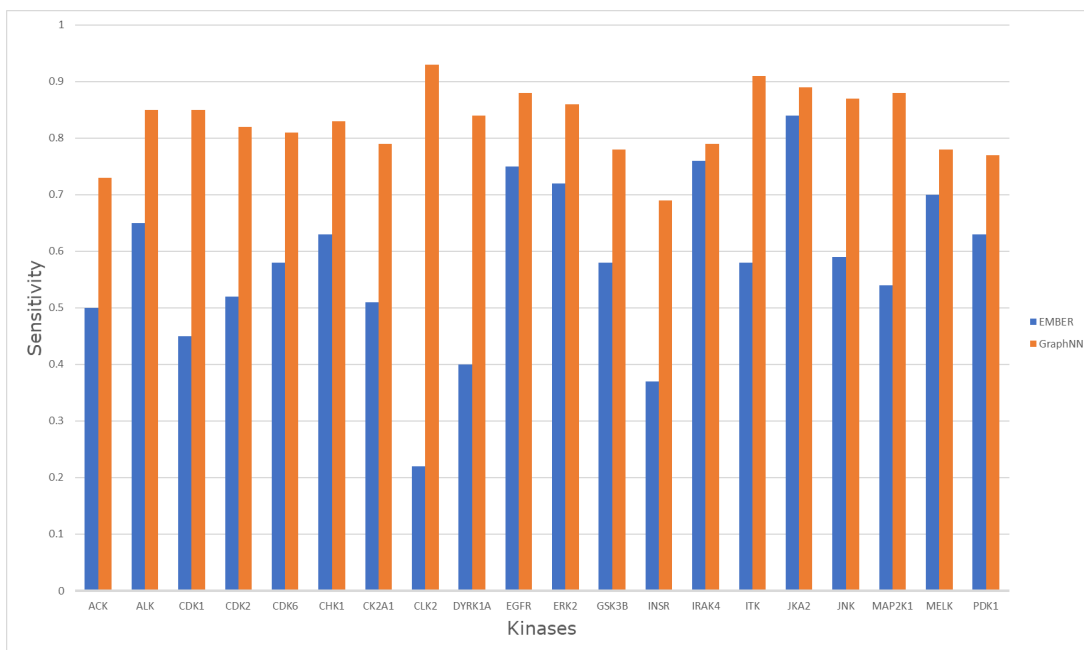


Figure 3: Comparison between EMBER and our approach based on GraphNN over sensitivity metric.

Protein	Bal. Accuracy	Sensitivity	F1-score	AUC
CDK1	0.928	0.954	0.277	0.974

Table 3: Results table for the single-class classifier

Protein	TP/P 1%	TP/P 2%	TP/P 5%	TP/P 10%	EF 1%	EF 2%	EF 5%	EF 10%
CDK1	34/109	58/109	109/109	100/109	31.19	26.60	2	9.11

Table 4: TP/P and EF values for 20 target classification

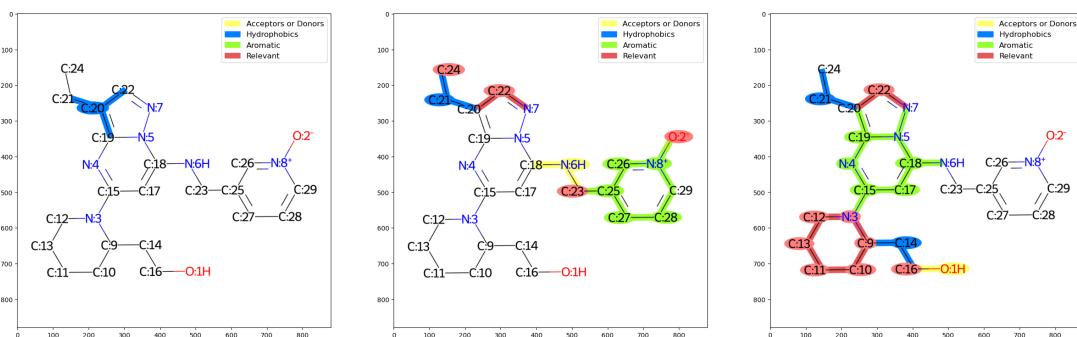


Figure 4: Visualisation of the relevant chemical groups in Dinaciclib (PubChem CID: 46926350). a) Single atom search b) Substructure investigation and c) Whole molecule analysis.

3 depths of explanation. Of particular interest is also the chemical interpretation attributed to each group, in fact the 3 different pharmacophoric categories and a fourth category within which all the relevant atoms will be placed. In fact, the H-bond acceptor or donor groups are highlighted in yellow, the hydrophobic groups in blue, and the aromatic groups in green. Lastly, the relevant atoms, which do not have explicit pharmacophoric functions but whose contribution in terms of bioactivity and/or stabilisation of the interaction with the binding site is highlighted, are highlighted in red.

The explanation was then tried on 19 CDK1 inhibitors, and the results has been compared to the docking results or experimental crystal structures of co-crystallised ligands (when available) for the same inhibitors. For 17 of 19 known drugs, our methodology is consistent with what was observed using experimental structures. and Table 1 shows which drug interactions were predicted by the proposed explainer. Figures 5 and 6 show an example of the information gathered during this phase of testing, which is shown in the supplementary material for all tested drugs. Interestingly, every "level" of depth of the convolution segment gives an important contribution to the final molecular interpretation. Indeed, as observed for Dinaciclib (Fig.1) the second step of depth (the one considering three atoms connected) is capable to catch important features as the H-bond donor N6, useful for the ligand protein complex stabilisation. Such a crucial information is then lost in the next step of the ligand interpretation (level7) where molecular substructures are considered. On the other hand, the higher level of molecular interpretation, is crucial to catch all the aromatic and lipophilic moieties that could be lost in

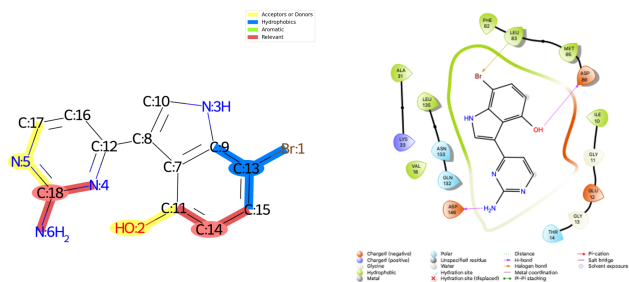


Figure 6: Comparison of the results obtained from the GRAD-CAM-like explainer versus molecular docking for Meridianin e.

molecular fingerprints can suffer for the correct interpretation of molecular moieties, especially for large and diverse chemical spaces datasets [25]. The combined use of different levels of molecular embeddings seems to be more and more efficient in catching crucial molecular features for the target assignment. The main strength of the presented approach is the combination of different layers of molecular embeddings (from single atom to complex structures). Every layer is capable to catch different aspects of a molecule, and every step enriches the others giving a complete interpretation of the molecule and of the moieties useful to interact with a specific target. As demonstrated in Fig. 4 for Dinaciclib, the complementarity of the layers is crucial in order not to lose chemical information. When going deeper on the explainability part of our method, it is clear that the proposed model is capable to rationally explain ligand moieties involved in the stabilisation of the host-guest interaction. For the majority of ligands analysed (17 out of 19), our method was in accordance with what observed using protein ligand complexes from experimental crystals or docking algorithms (when crystals were not available). In details, when the message passing mechanisms arrives to the third level, the entire structure is considered, accounting for 'regions' that actively contribute to the classification. Considering the whole structure of the molecules, instead of single atoms or small patterns really gives ideas about the important roles of the molecules to reach the target and bind to it strongly. For two compounds analysed, the method did not found relevant chemical parts to bind the CDK1 receptor. Given the nature of DL techniques used in this work, it is not possible to conclude why for these molecules the model failed. But for sure chemical structures of Flavopiridol and RGB286638 differ from the other structures. For the majority of molecular data in the training set, H-bond are mainly driven by nitrogen instead of oxygen, so probably the flavonoid structure of the FLavopiridol, is not easily read and interpreted by our network. Indeed, the molecular complexity of RGB286638 probably let the molecule to fall out of the applicability domain of the training and test set. For that reason, our model could fail in retrieving functional parts as interacting core. Similarly, Flavopiridol, a flavonoid derivatives, has a non common structure when compared to those in the initial dataset, while maintaining the h-bond acceptor/donor pattern useful for CDK1 binding.

Drug	Pubchem ID	GFP*	Accordance to docking
Flavopiridol	5287969	no	Hydrogen bond N:7 – ASP146; Pi-cation N:7 – TYR15; Hydrogen bond O:5H – GLU81; Hydrogen bond O:6 – LEU83;
Roscovitine	160355	yes	Hydrogen bond O:1H – ASN133; Hydrogen bond N:3H – LEU83; Pi-Pi interaction – LYS89;
RO3306	136240579	yes	Hydrogen bonds N:4H – O:3 – LEU83; Pi-Pi interaction – LYS89;
Dinaciclib	46926350	yes	Hydrogen bonds N:5 – N:6H – LEU83; Pi-Pi interaction – LYS89;
Milciclib	16718576	yes	Pi-Pi interaction – LYS89; Hydrogen bond O:1 – LYS33
Palbociclib	5330286	yes	Pi-Pi interaction – LYS89; Hydrogen bond N:8H – ASP86; Hydrogen bond O:2 – LYS33
Meriolin	24801699	yes	Hydrogen bond N:6H2 – ASP146; Hydrogen bond N:3H – LEU83
Variolin	9817550	yes	Hydrogen bonds N:3H – N:5H2 – LEU83; Hydrogen bond N:8H2 – ASP146;
Meridianin	9995236	yes	Hydrogen bond O:2H – ASP86; Halogen bond Br:1 – LEU83;
AZD5438	16747683	yes	Hydrogen bonds N:7H – N:8 – LEU83; Hydrogen bond O:2 <i>or</i> O:3 – ASP86
Roniciclib	45380979	yes	Hydrogen bond O:7H – LYS33; Hydrogen bonds N:9H – N:10 – LEU83; Hydrogen bond O:7H – LYS33;
SNS-032	3025986	yes	Hydrogen bonds N:8 – N:6H – LEU83; Hydrogen bond N:7 – LYS33;
Fostamatinib	11671467	yes	Pi-Pi interaction – LYS89; Hydrogen bond O:6H – O:7H – O:4 – LYS33;
AG-024322	135413565	yes	Hydrogen bond N:5 – LYS89; Hydrogen bond N:3H – SER84; Hydrogen bond N:4H – ASP89;
R547	6918852	yes	Hydrogen bond N:9H – ASP89; Hydrogen bond O:6 – LYS33;
RGB-286638	11285001	no	Hydrogen bond N:8 – LYS89; Hydrogen bond O:2 – GLN132; Hydrogen bond O:1 – LYS9;
ZK304709	59733314	yes	Pi-Pi interaction – LYS89; Hydrogen bond N:7H – GLU12; Hydrogen bond N:6 – GLU8;
JNJ-7706621	5330790	yes	Hydrogen bond N:12H2 – GLU81; Hydrogen bonds N:10 – N:7H – LEU83;
C26H31N7O**	46916588	yes	Pi-Pi interaction – LYS89; Hydrogen bonds N:7 – N:6H – LEU83;

*Guest Feature Prediction

**Molecular formula of 2-[[2S]-1-[8-ethyl-4-[(4-pyridin-2-ylphenyl)methylamino]pyrazolo[1,5-a][1,3,5]triazin-2-yl]piperidin-2-yl]ethanol

Table 5: Schematization of the **G**uest **F**eature **P**rediction (GFP) and for each of the 19 drugs tested. Black text depicts the interactions predicted in accordance with molecular docking, while red text indicate divergence

5 Conclusion

In the last years, Artificial Intelligence has been largely adopted in drug design virtual screening campaigns in order to strenghten predictions. The possibility of training models on

Drug	3 level XAI	7 level XAI	Accordance to docking
Flavopiridol	Hydrogen bond N:7 - ASP146; Pi-cation N:7 - TYR15; Hydrogen bond O:5H - GLU81; Hydrogen bond O:6 - LEU83;	Hydrogen bond N:7 - ASP146; Pi-cation N:7 - TYR15; Hydrogen bond O:5H - GLU81; Hydrogen bond O:6 - LEU83;	Hydrogen bond N:7 - ASP146; Pi-cation N:7 - TYR15; Hydrogen bond O:5H - GLU81; Hydrogen bond O:6 - LEU83;
Roscovitine	Hydrogen bond O:1H - ASN133; Hydrogen bond N:3H - LEU83; Pi-Pi interaction - LYS89;	Hydrogen bond O:1H - ASN133; Hydrogen bond N:3H - LEU83; Pi-Pi interaction - LYS89;	Hydrogen bond O:1H - ASN133; Hydrogen bond N:3H - LEU83; Pi-Pi interaction - LYS89;
RO3306	Hydrogen bonds N:4H - O:3 - LEU83; Pi-Pi interaction - LYS89;	Hydrogen bonds N:4H - O:3 - LEU83; Pi-Pi interaction - LYS89;	Hydrogen bonds N:4H - O:3 - LEU83; Pi-Pi interaction - LYS89;
Dinaciclib	Hydrogen bonds N:5 - N:6H - LEU83; Pi-Pi interaction - LYS89;	Hydrogen bonds N:5 - N:6H - LEU83; Pi-Pi interaction - LYS89;	Hydrogen bonds N:5 - N:6H - LEU83; Pi-Pi interaction - LYS89;
Miliciclib	Pi-Pi interaction - LYS89; Hydrogen bond O:1 - LYS33;	Pi-Pi interaction - LYS89; Hydrogen bond O:1 - LYS33	Pi-Pi interaction - LYS89; Hydrogen bond O:1 - LYS33
Palbociclib	Pi-Pi interaction - LYS89; Hydrogen bond N:8H - ASP86; Hydrogen bond O:2 - LYS33;	Pi-Pi interaction - LYS89; Hydrogen bond N:8H - ASP86; Hydrogen bond O:2 - LYS33;	Pi-Pi interaction - LYS89; Hydrogen bond N:8H - ASP86; Hydrogen bond O:2 - LYS33
Meriolin	Hydrogen bond N:6H2 - ASP146; Hydrogen bond N:3H - LEU83	Hydrogen bond N:6H2; Hydrogen bond N:3H - LEU83;	Hydrogen bond N:6H2; Hydrogen bond N:3H - LEU83
Variolin	Hydrogen bonds N:3H - N:5H2 - LEU83; Hydrogen bond N:8H2 - ASP146;	Hydrogen bonds N:3H - N:5H2 - LEU83; Hydrogen bond N:8H2 - ASP146;	Hydrogen bonds N:3H - N:5H2 - LEU83; Hydrogen bond N:8H2 - ASP146;
Meridianin	Hydrogen bond O:2H - ASP86; Halogen bond Br:1 - LEU83;	Hydrogen bond O:2H - ASP86; Halogen bond Br:1 - LEU83;	Hydrogen bond O:2H - ASP86; Halogen bond Br:1 - LEU83;
AZD5438	Hydrogen bonds N:7H - N:8 - LEU83; Hydrogen bond O:2 or O:3 - ASP86	Hydrogen bonds N:7H - N:8 - LEU83; Hydrogen bond O:2 or O:3 - ASP86	Hydrogen bonds N:7H - N:8 - LEU83; Hydrogen bond O:2 or O:3 - ASP86
Roniciclib	Hydrogen bond O:7H - LYS33; Hydrogen bonds N:9H - N:10 - LEU83; Hydrogen bond O:7H - LYS33;	Hydrogen bond O:7H - LYS33; Hydrogen bonds N:9H - N:10 - LEU83; Hydrogen bond O:7H - LYS33;	Hydrogen bond O:7H - LYS33; Hydrogen bonds N:9H - N:10 - LEU83; Hydrogen bond O:7H - LYS33;
SNS-032	Hydrogen bonds N:8 - N:6H - LEU83; Hydrogen bond N:7 - LYS33;	Hydrogen bonds N:8 - N:6H - LEU83; Hydrogen bond N:7 - LYS33;	Hydrogen bonds N:8 - N:6H - LEU83; Hydrogen bond N:7 - LYS33;
Postamatinib	Pi-Pi interaction - LYS89; Hydrogen bond O:6H - O:7H - O:4 - LYS33;	Pi-Pi interaction - LYS89; Hydrogen bond O:6H - O:7H - O:4 - LYS33;	Pi-Pi interaction - LYS89; Hydrogen bond O:6H - O:7H - O:4 - LYS33;
AG-024322	Hydrogen bond N:5 - LYS89; Hydrogen bond N:3H - SER84; Hydrogen bond N:4H - ASP89;	Hydrogen bond N:5 - LYS89; Hydrogen bond N:3H - SER84; Hydrogen bond N:4H - ASP89;	Hydrogen bond N:5 - LYS89; Hydrogen bond N:3H - SER84; Hydrogen bond N:4H - ASP89;
R547	Hydrogen bond N:9H - ASP89; Hydrogen bond O:6 - LYS33;	Hydrogen bond N:9H - ASP89; Hydrogen bond O:6 - LYS33;	Hydrogen bond N:9H - ASP89; Hydrogen bond O:6 - LYS33;
RGB-286638	Hydrogen bond N:8 - LYS89; Hydrogen bond O:2 - GLN132; Hydrogen bond O:1 - LYS9;	Hydrogen bond N:8 - LYS89; Hydrogen bond O:2 - GLN132; Hydrogen bond O:1 - LYS9;	Hydrogen bond N:8 - LYS89; Hydrogen bond O:2 - GLN132; Hydrogen bond O:1 - LYS9;
ZK304709	Pi-Pi interaction - LYS89; Hydrogen bond N:7H - GLU12; Hydrogen bond N:6 - GLU8;	Pi-Pi interaction - LYS89; Hydrogen bond N:7H - GLU12; Hydrogen bond N:6 - GLU8;	Pi-Pi interaction - LYS89; Hydrogen bond N:7H - GLU12; Hydrogen bond N:6 - GLU8;
JNJ-7706621	Hydrogen bond N:12H2 - GLU81; Hydrogen bonds N:10 - N:7H - LEU83;	Hydrogen bond N:12H2 - GLU81; Hydrogen bonds N:10 - N:7H - LEU83;	Hydrogen bond N:12H2 - GLU81; Hydrogen bonds N:10 - N:7H - LEU83;
C26H31N7O**	Pi-Pi interaction - LYS89; Hydrogen bonds N:7 - N:6H - LEU83;	Pi-Pi interaction - LYS89; Hydrogen bonds N:7 - N:6H - LEU83;	Pi-Pi interaction - LYS89; Hydrogen bonds N:7 - N:6H - LEU83;

*Guest Feature Prediction

**Molecular formula of 2-[(2S)-1-[8-ethyl-4-[(4-pyridin-2-ylphenyl)methylamino]pyrazolo[1,5-a][1,3,5]triazin-2-yl]piperidin-2-yl]ethanol

Table 6: Schematization of the **Guest Feature Prediction** (GFP) and for each of the 19 drugs tested. In black are shown the interactions predicted in accordance with molecular docking and in red the divergences.

known actives and inactives has been demonstrated to be a valuable tool to reduce false positives and catch molecular properties fundamental for ligand-protein interactions. The use of AI in chemoinformatics allowed the rise of ligand-based methods that were outclassed by structure-based methods in the last years. Structure-based methods offer the possibility to look deeper in the binding site of a protein allowing scientists to predict how ligand could bind to a specific target. Anyway, It is well known that the use of structure-based methods in drug design could be strongly affected by the protein and ligand conformation in retrieving important protein-ligand interactions. Moreover, high quality protein-ligand complexes are not always available

in public databases. Differently to structure-based methods, the results obtained from our method, enlighten not only the interacting partners but also the molecular moieties involved, for example, in the hydrophobic interactions (useful for entropy driven binding) and other chemical parts responsible for the recognition of CDK1. The main strength of our method is the use of combined molecular embeddings layers that taken together are capable to account the whole molecular structure and functional groups connections. As a result of this architecture, it is possible to correctly assign a target to each molecule and retrieve the main molecule moieties involved in the target assignation/binding. Such a data is not retrievable in other computational techniques used for virtual screening, letting our method to unveil hidden molecular moieties useful for binding a specific target. Our methods herein presented, will be applied to other targets and molecules prioritised by graph-ember will be tested on a panel of kinases in order to experimentally validate the approach.

Supplementary information

A detailed description of the predictive results obtained from the Hierarchical Gradient Explainer, (HGE) approach for all 19 approved CDK1 drugs is provided in the attached file “supplementary_material.pdf”.

Abbreviations

- CADD. Computer-Aided Drug Design
- VS. Virtual Screening
- SAR. Structure Activity Relationship
- XAI. Explainable AI
- EMBER. EMBedding multiple molecular fingeRprints
- IC50. Half Maximal Inhibitory Concentration
- Ki. Inhibition constant
- Kd. Dissociation constant
- MLP. Multi Layer Perceptron
- PDB. Protein Data Bank
- ReLU. Rectified Linear Unit
- wBCE. Weighted Binary Cross-Entropy
- Grad-CAM. Gradient-weighted Class Activation Mapping
- TP. True Positive
- P. Positive

- TN. True Negative
- N. Negative
- TP/P. True Positive vs Positive ratio
- EF. Enrichment Factor

References

- [1] ChEMBL Database. <https://www.ebi.ac.uk/chembl/>. Accessed: 24/09/2018.
- [2] Azizeh Abdolmaleki, Jahan B. Ghasemi, and Fatemeh Ghasemi. Computer aided drug design for multi-target drug design: Sar /qsar, molecular docking and pharmacophore methods. *Current Drug Targets*, 18(5):556–575, April 2017.
- [3] Meriem Bahi and Mohamed Batouche. Deep learning for ligand-based virtual screening in drug discovery. In *2018 3rd International Conference on Pattern Analysis and Intelligent Systems (PAIS)*, pages 1–5, 2018.
- [4] Kristy A Carpenter, David S Cohen, Juliet T Jarrell, and Xudong Huang. Deep learning and virtual drug screening. *Future Medicinal Chemistry*, 10(21):2557–2567, 2018. PMID: 30288997.
- [5] Xin Chen, Xien Liu, and Ji Wu. Drug-drug interaction prediction with graph representation learning. In *2019 IEEE International Conference on Bioinformatics and Biomedicine (BIBM)*, page 354–361, November 2019.
- [6] Pitchai Daisy, Sanjeev Kumar Singh, Periyasamy Vijayalakshmi, Chandrabose Selvaraj, Manikkam Rajalakshmi, and Sukumaran Suveena. A database for the predicted pharmacophoric features of medicinal compounds. *Bioinformation*, 6(4):167–168, May 2011.
- [7] Alexej Dick and Simon Cocklin. Bioisosteric replacement as a tool in anti-hiv drug design. *Pharmaceuticals*, 13(33):36, March 2020.
- [8] Justin Gilmer, Samuel S Schoenholz, Patrick F Riley, Oriol Vinyals, and George E Dahl. Neural message passing for quantum chemistry. In *International conference on machine learning*, pages 1263–1272. PMLR, 2017.
- [9] Steven Kearnes, Kevin McCloskey, Marc Berndl, Vijay Pande, and Patrick Riley. Molecular graph convolutions: moving beyond fingerprints. *Journal of Computer-Aided Molecular Design*, 30(8):595–608, August 2016.
- [10] György M. Keserű and Gergely M. Makara. Hit discovery and hit-to-lead approaches. *Drug Discovery Today*, 11(15):741–748, August 2006.
- [11] Talia B. Kimber, Yonghui Chen, and Andrea Volkamer. Deep learning in virtual screening: Recent applications and developments. *International Journal of Molecular Sciences*, 22(9):4435, April 2021.
- [12] Thomas N Kipf and Max Welling. Semi-supervised classification with graph convolutional networks. *arXiv preprint arXiv:1609.02907*, 2016.

- [13] Fang-Yu Lin and Alexander D. MacKerell. *Force Fields for Small Molecules*, volume 2022 of *Methods in Molecular Biology*, page 21–54. Springer New York, New York, NY, 2019.
- [14] Isabella Mendolia, Salvatore Contino, Giada De Simone, Ugo Perricone, and Roberto Pirrone. Ember—embedding multiple molecular fingerprints for virtual screening. *International Journal of Molecular Sciences*, 23(44):2156, Jan 2022.
- [15] Christopher Morris, Martin Ritzert, Matthias Fey, William L Hamilton, Jan Eric Lenssen, Gaurav Rattan, and Martin Grohe. Weisfeiler and leman go neural: Higher-order graph neural networks. In *Proceedings of the AAAI conference on artificial intelligence*, volume 33, pages 4602–4609, 2019.
- [16] Phillip E. Pope, Soheil Kolouri, Mohammad Rostami, Charles E. Martin, and Heiko Hoffmann. Explainability methods for graph convolutional neural networks. *2019 IEEE/CVF Conference on Computer Vision and Pattern Recognition (CVPR)*, pages 10764–10773, 2019.
- [17] Olaf Ronneberger, Philipp Fischer, and Thomas Brox. U-net: Convolutional networks for biomedical image segmentation. In *Medical Image Computing and Computer-Assisted Intervention—MICCAI 2015: 18th International Conference, Munich, Germany, October 5–9, 2015, Proceedings, Part III 18*, pages 234–241. Springer, 2015.
- [18] Franco Scarselli, Marco Gori, Ah Chung Tsoi, Markus Hagenbuchner, and Gabriele Monfardini. The graph neural network model. *IEEE Transactions on Neural Networks*, 20(1):61–80, 2009.
- [19] Ramprasaath R. Selvaraju, Michael Cogswell, Abhishek Das, Ramakrishna Vedantam, Devi Parikh, and Dhruv Batra. Grad-cam: Visual explanations from deep networks via gradient-based localization. *International Journal of Computer Vision*, 128(2):336–359, Feb 2020. arXiv:1610.02391 [cs].
- [20] Jonathan M. Stokes, Kevin Yang, Kyle Swanson, Wengong Jin, Andres Cubillos-Ruiz, Nina M. Donghia, Craig R. MacNair, Shawn French, Lindsey A. Carfrae, Zohar Bloom-Ackermann, Victoria M. Tran, Anush Chiappino-Pepe, Ahmed H. Badran, Ian W. Andrews, Emma J. Chory, George M. Church, Eric D. Brown, Tommi S. Jaakkola, Regina Barzilay, and James J. Collins. A deep learning approach to antibiotic discovery. *Cell*, 180(4):688–702.e13, 2020.
- [21] Shan Sun and David J. Huggins. Assessing the effect of forcefield parameter sets on the accuracy of relative binding free energy calculations. *Frontiers in Molecular Biosciences*, 9:972162, September 2022.
- [22] Thomas Unterthiner, Andreas Mayr, and Jörg Kurt Wegner. Deep learning as an opportunity in virtual screening. 2015.
- [23] Shudong Wang, Zhenzhen Du, Mao Ding, Alfonso Rodriguez-Paton, and Tao Song. Kg-dti: a knowledge graph based deep learning method for drug-target interaction predictions and alzheimer’s disease drug repositions. *Applied Intelligence*, 52(1):846–857, January 2022.
- [24] Zhenqin Wu, Bharath Ramsundar, Evan N Feinberg, Joseph Gomes, Caleb Geniesse, Aneesh S Pappu, Karl Leswing, and Vijay Pande. Moleculenet: a benchmark for molecular machine learning. *Chemical science*, 9(2):513–530, 2018.

- [25] Jingbo Yang, Yiyang Cai, Kairui Zhao, Hongbo Xie, and Xiujie Chen. Concepts and applications of chemical fingerprint for hit and lead screening. *Drug Discovery Today*, 27(11):103356, 2022.
- [26] Kevin Yang, Kyle Swanson, Wengong Jin, Connor Coley, Philipp Eiden, Hua Gao, Angel Guzman-Perez, Timothy Hopper, Brian Kelley, Miriam Mathea, Andrew Palmer, Volker Settels, Tommi Jaakkola, Klavs Jensen, and Regina Barzilay. Analyzing learned molecular representations for property prediction. *Journal of Chemical Information and Modeling*, 59(8):3370–3388, 2019. PMID: 31361484.
- [27] Zhitao Ying, Dylan Bourgeois, Jiaxuan You, Marinka Zitnik, and Jure Leskovec. Gnnexplainer: Generating explanations for graph neural networks. *Advances in neural information processing systems*, 32, 2019.
- [28] Xiangxiang Zeng, Xinqi Tu, Yuansheng Liu, Xiangzheng Fu, and Yansen Su. Toward better drug discovery with knowledge graph. 72:114–126, February 2022.
- [29] Jie Zhou, Ganqu Cui, Shengding Hu, Zhengyan Zhang, Cheng Yang, Zhiyuan Liu, Lifeng Wang, Changcheng Li, and Maosong Sun. Graph neural networks: A review of methods and applications. *AI Open*, 1:57–81, 2020.